Focused ion beam milling of gallium phosphide nanostructures for photonic applications

Eleonora De Luca,[1,3] Reza Sanatinia,[2] Srinivasan Anand,[2] and Marcin Swillo[1*]

[1] *School of Engineering Sciences (SCI), KTH Royal Institute of Technology, Roslagstullsbacken 21, SE-10691 Stockholm, Sweden*

[2] *School of Information and Communication Technology, KTH Royal Institute of Technology, Electrum 229, SE-16440 Kista, Sweden*

[3]*eldl@kth.se*

[*]*marcin@kth.se*

Abstract: We report on the fabrication of gallium phosphide (GaP) nanowaveguides of controlled dimensions, as small as 0.03 μm and aspect ratio in excess of 20, using focused ion beam (FIB) milling. A known limitation of this fabrication process for photonic applications is the formation of gallium droplets on the surface. We demonstrate a post-fabrication step using a pulsed laser to locally oxidize the excess surface gallium on the FIB milled nanostructures. The process significantly reduces the waveguide losses. The surface optical quality of the fabricated GaP nanowaveguides has been evaluated by second-harmonic generation experiments. Surface and bulk contributions to second-order optical nonlinearities have been identified by polarization measurements. The presented method can potentially be applied to other III-V nanostructures to reduce optical losses.

©2016 Optical Society of America

OCIS codes: (160.6000) Semiconductor materials; (350.3850) Materials processing; (190.4400) Nonlinear optics, materials; (190.4350) Nonlinear optics at surfaces; (230.7370) Waveguides; (190.2620) Harmonic generation and mixing; (350.4238) Nanophotonics and photonic crystals.

References and links

1. M. Komuro, "Ion beam exposure apparatus using a liquid metal source," Thin Solid Films **92**(1-2), 155–164 (1982).
2. R. L. Kubena, R. L. Seliger, and E. H. Stevens, "High resolution sputtering using a focused ion beam," Thin Solid Films **92**(1–2), 165–169 (1982).
3. T. Liang, A. Stivers, R. Livengood, P.-Y. Yan, G. Zhang, and F.-C. Lo, "Progress in extreme ultraviolet mask repair using a focused ion beam," J. Vac. Sci. Technol. B Microelectron. Nanom. Struct. **18**(6), 3216 (2000).
4. A. Al-Abboodi, J. Fu, P. M. Doran, and P. P. Y. Chan, "Three-dimensional nanocharacterization of porous hydrogel with ion and electron beams," Biotechnol. Bioeng. **110**(1), 318–326 (2013).
5. K. Narayan, C. M. Danielson, K. Lagarec, B. C. Lowekamp, P. Coffman, A. Laquerre, M. W. Phaneuf, T. J. Hope, and S. Subramaniam, "Multi-resolution correlative focused ion beam scanning electron microscopy: applications to cell biology," J. Struct. Biol. **185**(3), 278–284 (2014).
6. X. Jiang, Q. Gu, F. Wang, J. Lv, Z. Ma, and G. Si, "Fabrication of coaxial plasmonic crystals by focused ion beam milling and electron-beam lithography," Mater. Lett. **100**, 192–194 (2013).
7. M. A. Draganski, E. Finkman, B. C. Gibson, B. A. Fairchild, K. Ganesan, N. Nabatova-Gabain, S. Tomljenovic-Hanic, A. D. Greentree, and S. Prawer, "Tailoring the optical constants of diamond by ion implantation," Opt. Mater. Express **2**(5), 644 (2012).
8. Y. L. D. Ho, R. Gibson, C. Y. Hu, M. J. Cryan, J. G. Rarity, P. J. Heard, J. A. Timpson, A. M. Fox, M. S. Skolnick, M. Hopkinson, and A. Tahraoui, "Focused ion beam etching for the fabrication of micropillar microcavities made of III-V semiconductor materials," J. Vac. Sci. Technol. B Microelectron. Nanom. Struct. **25**(4), 1197 (2007).
9. X. Jiang, Q. Gu, L. Yang, R. Zhao, J. Lv, Z. Ma, and G. Si, "Functional plasmonic crystal nanoantennae with ultrasmall gaps and highly tunable profiles," Opt. Laser Technol. **71**, 1–5 (2015).
10. R. W. Tjerkstra, F. B. Segerink, J. J. Kelly, and W. L. Vos, "Fabrication of three-dimensional nanostructures by focused ion beam milling," J. Vac. Sci. Technol. B Microelectron. Nanom. Struct. **26**(3), 973 (2008).
11. D. C. Aveline, L. Baumgartel, B. Ahn, and N. Yu, "Focused ion beam engineered whispering gallery mode resonators with open cavity structure," Opt. Express **20**(16), 18091–18096 (2012).

#255882 Received 17 Dec 2015; revised 19 Jan 2016; accepted 19 Jan 2016; published 22 Jan 2016

12. D. Freeman, S. Madden, and B. Luther-Davies, “Fabrication of planar photonic crystals in a chalcogenide glass using a focused ion beam,” Opt. Express **13**(8), 3079–3086 (2005).
13. F. Vallini, D. S. L. Figueira, P. F. Jarschel, L. A. M. Barea, A. A. G. Von Zuben, and N. C. Frateschi, “Effects of Ga+ milling on InGaAsP quantum well laser with mirrors milled by focused ion beam,” J. Vac. Sci. Technol. B Microelectron. Nanom. Struct. **27**(5), L25 (2009).
14. L. A. M. Barea, F. Vallini, A. R. Vaz, J. R. Mialichi, and N. C. Frateschi, “Low-roughness active microdisk resonators fabricated by focused ion beam,” J. Vac. Sci. Technol. B Microelectron. Nanom. Struct. **27**(6), 2979 (2009).
15. J. Daniel and D. F. Moore, “A microaccelerometer structure fabricated in silicon-on-insulator using a focused ion beam process,” Sens. Actuators A Phys. **73**(3), 201–209 (1999).
16. J. Teng and P. Prewett, “Focused ion beam fabrication of thermally actuated bimorph cantilevers,” Sens. Actuators A Phys. **123–124**, 608–613 (2005).
17. B. P. Gila, “Applications of new focused ion beams in nanofabrication and material studies,” Microsc. Anal. (Am. Ed.) **7**, 7–10 (2013).
18. T. Fujii, K. Iwasaki, M. Munekane, T. Takeuchi, M. Hasuda, T. Asahata, M. Kiyohara, T. Kogure, Y. Kijima, and T. Kaito, “A nanofactory by focused ion beam,” J. Micromech. Microeng. **15**(10), S286–S291 (2005).
19. J. Gierak, A. Madouri, A. L. Biance, E. Bourhis, G. Patriarche, C. Ulysse, D. Lucot, X. Lafosse, L. Auvray, L. Bruchhaus, and R. Jede, “Sub-5nm FIB direct patterning of nanodevices,” Microelectron. Eng. **84**(5–8), 779–783 (2007).
20. J. H. Wu, W. Ye, B. L. Cardozo, D. Saltzman, K. Sun, H. Sun, J. F. Mansfield, R. S. Goldman, J. H. Wu, W. Ye, B. L. Cardozo, D. Saltzman, K. Sun, H. Sun, and J. F. Mansfield, “Formation and coarsening of Ga droplets on focused-ion-beam irradiated GaAs surfaces,” Appl. Phys. Lett. **95**(15), 153107 (2009).
21. Transparency Market Research, “Focused Ion Beam Market - Global Industry Analysis, Size, Share, Growth, Trends and Forecast 2015 - 2021,” (2015) http://www.transparencymarketresearch.com/focused-ion-beam-market.html.
22. M. C. Dolph and C. Santeufemio, “Exploring cryogenic focused ion beam milling as a Group III–V device fabrication tool,” Nucl. Instruments Methods Phys. Res. Sect. B Beam Interact. with Mater. Atoms **328**, 33–41 (2014).
23. I. Shoji, T. Kondo, A. Kitamoto, M. Shirane, and R. Ito, “Absolute scale of second-order nonlinear-optical coefficients,” J. Opt. Soc. Am. B **14**(9), 2268–2294 (1997).
24. Y. A. Goldbery, *Handobook Series on Semiconductor Parameters* (World Scientific, 1996).
25. D. E. Aspnes and A. A. Studna, “Dielectric functions and optical parameters of Si, Ge, GaP, GaAs, GaSb, InP, InAs, and InSb from 1.5 to 6.0 eV,” Phys. Rev. B **27**(2), 985–1009 (1983).
26. R. Sanatinia, M. Swillo, and S. Anand, “Surface second-harmonic generation from vertical GaP nanopillars,” Nano Lett. **12**(2), 820–826 (2012).
27. A. Dobrovolsky, P. O. Å. Persson, S. Sukrittanon, Y. Kuang, C. W. Tu, W. M. Chen, and I. A. Buyanova, “Effects of Polytypism on Optical Properties and Band Structure of Individual Ga(N)P Nanowires from Correlative Spatially Resolved Structural and Optical Studies,” Nano Lett. **15**(6), 4052–4058 (2015).
28. Q. Wu, Z. Hu, C. Liu, X. Wang, Y. Chen, and Y. Lu, “Synthesis and optical properties of gallium phosphide nanotubes,” J. Phys. Chem. B **109**(42), 19719–19722 (2005).
29. R. Sanatinia, S. Anand, and M. Swillo, “Experimental quantification of surface optical nonlinearity in GaP nanopillar waveguides,” Opt. Express **23**(2), 756–764 (2015).
30. R. Sanatinia, S. Anand, and M. Swillo, “Modal Engineering of Second-Harmonic Generation in Single GaP Nanopillars,” Nano Lett. **14**(9), 5376–5381 (2014).
31. K. Rivoire, Z. Lin, F. Hatami, W. T. Masselink, and J. Vucković, “Second harmonic generation in gallium phosphide photonic crystal nanocavities with ultralow continuous wave pump power,” Opt. Express **17**(25), 22609–22615 (2009).
32. K. Rivoire, S. Buckley, F. Hatami, and J. Vučković, “Second harmonic generation in GaP photonic crystal waveguides,” Appl. Phys. Lett. **98**(26), 98–101 (2011).
33. G. Shambat, K. Rivoire, J. Lu, F. Hatami, and J. Vucković, “Tunable-wavelength second harmonic generation from GaP photonic crystal cavities coupled to fiber tapers,” Opt. Express **18**(12), 12176–12184 (2010).
34. S.-L. Ou, D.-S. Wuu, Y.-C. Fu, S.-P. Liu, R.-H. Horng, L. Liu, and Z.-C. Feng, “Growth and etching characteristics of gallium oxide thin films by pulsed laser deposition,” Mater. Chem. Phys. **133**(2–3), 700–705 (2012).
35. E. Millon, “Advanced functional oxide thin films grown by pulsed-laser deposition,” Appl. Surf. Sci. **278**, 2–6 (2013).
36. C. Hebert, A. Petitmangin, J. Perrière, E. Millon, A. Petit, L. Binet, and P. Barboux, “Phase separation in oxygen deficient gallium oxide films grown by pulsed-laser deposition,” Mater. Chem. Phys. **133**(1), 135–139 (2012).
37. F.-P. Yu, S.-L. Ou, and D.-S. Wuu, “Pulsed laser deposition of gallium oxide films for high performance solar-blind photodetectors,” Opt. Mater. Express **5**(5), 1240–1249 (2015).

Introduction

Focused ion beam (FIB) technology has become increasingly attractive since the introduction of the liquid metal ion source (LMIS) [1,2]. Today, FIB is an appealing tool in different

#255882 Received 17 Dec 2015; revised 19 Jan 2016; accepted 19 Jan 2016; published 22 Jan 2016
© 2016 OSA

research areas: in the semiconductor and electronics industry [3], life sciences [4,5], optics and photonics applications [6–14] and micro-electromechanical systems (MEMS) [15,16].

The diffusion of FIB technology for different applications has largely been due to its several features, namely choice of ion species [17], variable ion current [8,9,15] and ion energy and injected gases [3,15]. The same tool allows imaging [4,5], (gas assisted) milling [3–5,8–19], gas assisted deposition [3,15] and implantation [7] of a selected sample. Moreover, a wide range of materials such as semiconductors [8,10,17,19], metals [3,6,9], soft materials [4,5] and insulators [7,11,12,18] can be processed by FIB. In addition, it offers a maskless fabrication process combined with the possibility of very fine focusing and high resolution. The combination of all these factors allows the fabrication of structures with complex geometries [10,18], small features down to sub-5 nm dimensions [5,19] and high aspect ratios [6]. However, when energetic ions hit the target, a variety of ion-solid interactions can occur, causing sputtering, surface amorphization, implantation, swelling, deposition, backscattering and nuclear reactions. In addition, FIB milling of III-V compounds results in appreciable residual group-III species on the surface, often in the form of droplets [17,20]. This phenomenon is well known for Ga^+ ion beam milling, which is the most commonly used technique [21]. Attempts to avoid the formation of the III-material-rich droplets have been made by milling at cryogenic temperatures but without success [22]. After the FIB milling it is possible to partially recover the samples by thermal annealing, usually performed at temperatures ranging from 200 °C to 600 °C [13].

Among different III-V compounds, gallium phosphide (GaP) has a high second order nonlinear coefficient [23], high thermal conductivity [24] and a broad transparency range [25], which make it an excellent material for nonlinear optical applications. Moreover, it has a high refractive index [25], which enhances the rapid variation of electric field across GaP/ air interfaces, contributing to the strong surface optical nonlinearity. GaP has been widely employed for photonics applications, especially in its nanopillar and nanotube shapes [26–30], but other examples of geometries are reported as well [10, 31–33].

In this paper, we present the fabrication of GaP multilayer slab waveguides (MSWs) by FIB. A post-fabrication step in which the FIB milled MSWs are treated by pulsed laser irradiation in ambient air is used to recover the optical properties by oxidising the surfaces gallium droplets. By measuring the second harmonic generation (SHG) of light from the MSWs, we demonstrate that this fabrication procedure guarantees high second-order nonlinear optical properties of the structures, including but not limited to the surface properties.

Focused ion beam fabrication

A dual-beam FIB machine FEI Nova 200 has been used for fabricating the structures. This system contained both a tilted ion beam column and a vertical electron column, which allowed real time monitoring and non-destructive characterization by scanning electron microscope (SEM). The ion beam was generated from a Ga^+ liquid metal source. For the experiments reported here, the acceleration voltage was set at 30 kV; the FIB milling currents at 10 pA and 50 pA corresponding to a nominal beam diameter of 12 nm and 19 nm, respectively. We note that the FIB current can affect the implantation characteristics as well as the amount of gallium generated. However, our primary purpose to use the higher current was to fabricate structures in a shorter time and/or with larger heights. The dwell time was defined at a value of 20 μs. Samples of undoped (100) GaP were used.

Two types of structures have been fabricated (Fig. 1). The first type (I) (Fig. 1(a)-1(b)) was a MSW fabricated at ion beam current of 10 pA, consisting of parallel lines of width w_n = (0.45 ± 0.05) μm and length l = (4.90 ± 0.05) μm, 50% duty cycle and height h = (1.10 ± 0.01) μm. Here, w_n represents the average between the top and at the bottom widths, as measured from the top-view SEM images. MSW (I) was made of parallel slabs with the same dimensions and spacing, as a standard waveguide. The interest for the structure derived from

#255882 Received 17 Dec 2015; revised 19 Jan 2016; accepted 19 Jan 2016; published 22 Jan 2016
© 2016 OSA

the possibility to compare the optical response in the same conditions for each of the slabs. The second MSW (II) (Fig. 1- (c-d)), has been realised in two versions by using ion beam currents of 10 pA and 50 pA. They were fabricated as a progression of widths of the slabs to investigate the dependence on geometrical dimensions on surface and bulk optical nonlinearities. The structure fabricated with ion beam current of 10 pA ranged from w_n = (0.04 ± 0.01) µm to w_n = (0.40 ± 0.05) µm, length l = (5.10 ± 0.05) µm and height h = (0.30 ± 0.01) µm. On the other hand, MSW (II) fabricated at 50 pA, ranged from w_n = (0.03 ± 0.01) µm to w_n = (0.42 ± 0.07) µm, length l = (5.05 ± 0.05) µm and height increasing from h = (0.60 ± 0.01) µm to h = (1.30 ± 0.01) µm corresponding to the smallest and the largest slab, respectively. The best aspect ratio achieved was approximately 20. Both types of structure were patterned parallel to the crystallographic axis of GaP wafer, i.e. 45° rotated respect to the cleaving edges of the samples.

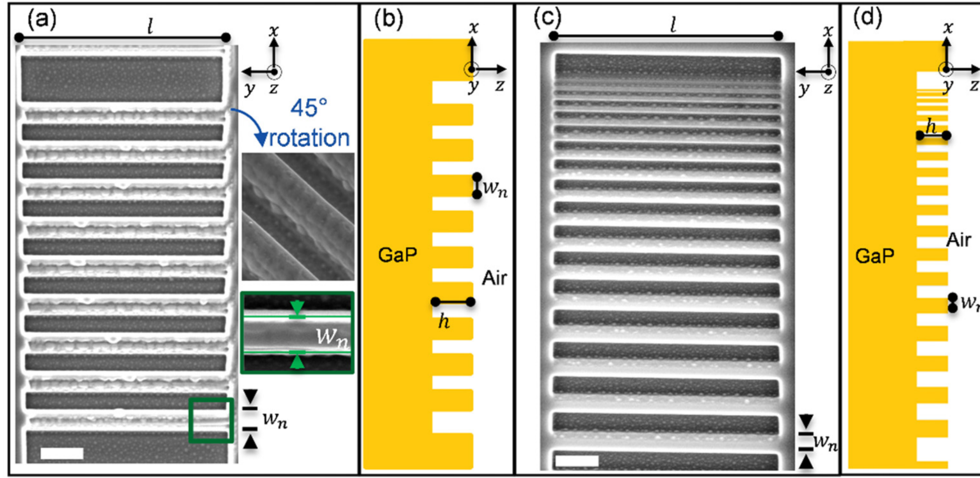

Fig. 1. Fabricated GaP multilayer slab waveguides. Indicated scale bars 1 µm. (a) SEM picture of the structure type I (fabricated at 10 pA FIB current). The insets show magnified view of the structure where w_n represents the average width of the waveguide. (b) Schematics of type I. (c) SEM picture of the structure type II (fabricated at 10 pA FIB current). (d) Schematics of type II.

Analysis of second-order optical nonlinearity

For GaP and all the crystals with $\bar{4}3m$ symmetry, the only nonzero components of the second-order nonlinear susceptibility tensor are $d_{14} = d_{25} = d_{36} = d$. Therefore, the second-order nonlinear polarization along the crystallographic axes are as follows [30]:

$$P_x^{(2)} = 2dE_yE_z = 2dE_TE_z \sin\varphi_{PUMP} \tag{1}$$

$$P_y^{(2)} = 2dE_zE_x = 2dE_TE_z \cos\varphi_{PUMP} \tag{2}$$

$$P_z^{(2)} = 2dE_xE_y = d\left(E_T\right)^2 \sin 2\varphi_{PUMP} \tag{3}$$

where E_T and E_z are the transverse (xy-plane) and the longitudinal electric field of the guided pump respectively, φ_{PUMP} is the angle between the pump polarization and the x-axis in the xy-plane. Two possible cases have to be considered: (a) φ_{PUMP} = 0°, i.e. the pump polarization is along the crystallographic x-axis and (b) the pump is oriented at φ_{PUMP} = 45°. In case (a), the only nonzero second-order nonlinear polarization is given by Eq. (2); in case (b), two

#255882 Received 17 Dec 2015; revised 19 Jan 2016; accepted 19 Jan 2016; published 22 Jan 2016

transversal component, i.e. $P_x^{(2)} = \sqrt{2}\, dE_T E_z$ and $P_y^{(2)} = \sqrt{2}\, dE_T E_z$, and longitudinal component $P_z^{(2)} = d\, E_T^2$, are present.

Furthermore, at the surface, the inversion symmetry is broken, resulting in new nonzero elements of the nonlinear susceptibility tensor. Both material and field discontinuities contribute to the surface nonlinearity. If the x-axis is orthogonal to the surface of the crystal with $\bar{4}3$ m symmetry, the second-order nonlinear susceptibility tensor [29] can be defined as:

$$d_S = \begin{bmatrix} d_{11}^s & d_{12}^s & d_{13}^s & d_{14}^s & 0 & 0 \\ 0 & 0 & 0 & 0 & d_{25}^s & d_{26}^s \\ 0 & 0 & 0 & 0 & d_{35}^s & d_{36}^s \end{bmatrix} \tag{4}$$

In case (a) $\varphi_{PUMP} = 0°$, tensor in Eq. (4) leads to the second-order nonlinear polarization at the surface $P_x^{(2)} = d^S{}_{11}\, E_x^2$.

Considering the symmetry of the transverse and longitudinal components for the guided pump in the mode TM_0 and case (a), the nonlinear polarization density can excite two modes at the SHG wavelength, TM_1 and TE_1, respectively related to the surface and the bulk contributions to the nonlinear polarization. Since $P_y^{(2)}$, results in a SHG light with polarization perpendicular to the pump and $P_x^{(2)}$, results in a SHG light with the same polarization of the pump, it is possible to identify bulk and surface contributions by polarization measurements.

In case (b), the pump is linearly polarized at 45° respect to the crystallographic axis. Therefore, it is guided in a superposition of TM_0 and TE_0 modes. Hence, the polarization of the SHG light depends on the phase-matching condition between the pump guided in TM_0 and TE_0 modes and SHG light guided in TM_1 and TE_1.

Second-harmonic generation measurements

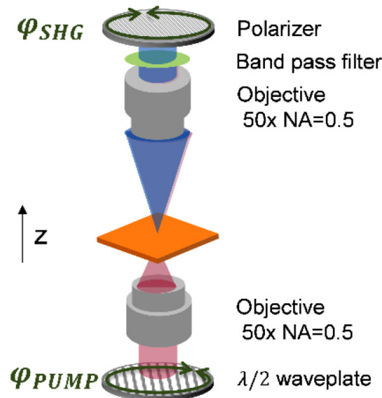

Fig. 2. Optical setup for the polarization measurements of the SHG light.

A Ti:Sapphire laser with 100 fs pulses and a central wavelength of 840 nm at 82 MHz repetition rate was used as the pump for the second harmonic generation in the transmission configuration setup reported in Fig. 2. The laser beam passed through a rotatable half-wave plate that allowed to rotate the linear polarization of the pump and, successively, was focused by a 50x Olympus microscope objective, with NA = 0.5. The incident pump propagated along the crystallographic z-axis of the sample with an average diameter of 2 µm on the top surface. The generated SH light was collected by a 50x Olympus objective, with NA = 0.5 and the collimated beam was passing through a Schott Glass band pass filter BG39 (blocking pump wavelength) and a rotatable polarizer. This setup allowed the measurement of SHG light in two different configurations: (i) parallel to the pump and (ii) orthogonal to the pump, which correspond to $\varphi_{SHG} = \varphi_{PUMP}$ and $\varphi_{SHG} = \varphi_{PUMP} + 90°$, respectively. The SHG light was coupled

#255882 Received 17 Dec 2015; revised 19 Jan 2016; accepted 19 Jan 2016; published 22 Jan 2016
© 2016 OSA

to a multimode fiber and guided to a monochromator, set at 420 nm. Finally, a Perkin Elmer silicon avalanche photodiode was used to measure the intensity of the SHG light.

As a post-processing step, the same pump laser was used to expose the samples with an average power of 150 mW and a constant polarization (case (a), $\varphi_{PUMP} = 0°$).

For short time exposure, below 5 min, MSW (I) was tested. In this case, the SHG signal increased above 200% from the initial value (Fig. 3-a). Since the MSW(I) was 450 nm wide, no contribution from the surface to the SHG light was observed.

In contrast to MSW (I), for MSW (II) fabricated at 50 pA it was not possible to measure any SH generated signal. To recover the structure, additional process steps were necessary. The process cycle consisted of fast scanning of the entire structure with the laser (~2 s per spot, 150 mW), oxygen plasma cleaning and hydrofluoric acid (HF) wet etching. After two such process cycles SHG measurements were performed and Fig. 3(b) shows SHG light intensity as a function of laser exposure time (150 mW average power). In this case, the polarizer for SHG light was rotated from parallel to orthogonal configurations in each measurement. This allowed the observation of contemporary evolution of the bulk and the surface contributions to the SHG light. The graph presented in Fig. 3(b) shows increase of the bulk contribution above 200% of the initial value. At the same time, the surface contribution to the SHG light stabilized at about 25% of the initial value. It was possible to observe an increasing bulk contribution to SHG light and a reduction of the surface contribution, which we attributed to an oxidization process. Oxidation of the surface leads to reduced electric field gradient and modification of material discontinuity at the interface between gallium phosphide and air.

Concerning the SHG measured in Fig. 3, we note that in Fig. 3(a), the intensity fluctuations are due to dynamic thermal effects, such as absorption by gallium droplets, chemical modifications and possible redistribution of surface gallium. In the case of Fig. 3(b), the reduction of the intensity after ~37 min is due to laser-induced damage of the waveguides.

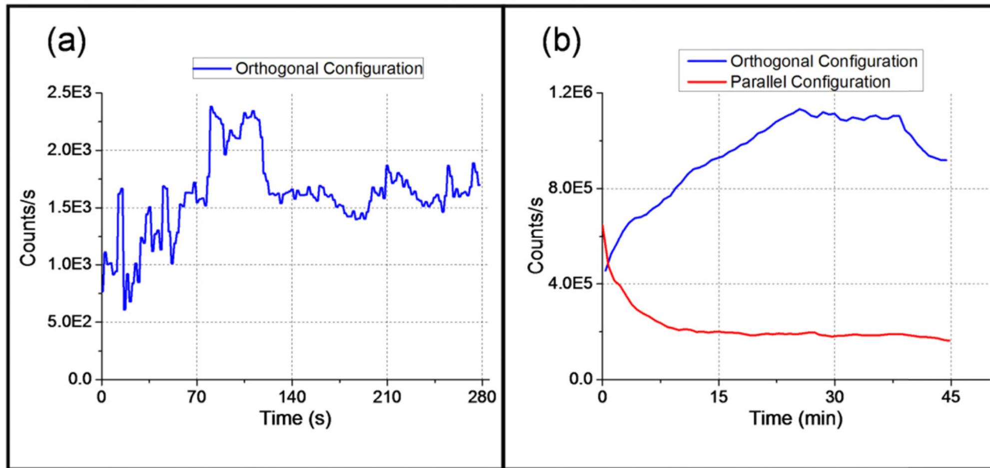

Fig. 3. SHG intensity for pulsed-laser exposure with average power P_{av} = 150mW. (Blue line) bulk contribution to the SHG light, (red line) surface contribution to the SHG light. (a) MSW (I) (fabricated at 10 pA FIB current), waveguide width w_n = (450 ± 50) nm. (b) MSW (II) (fabricated at 50pA FIB current), waveguide width w_n = (280 ± 10) nm.

Nonlinear properties of the fabricated samples, specifically the bulk and surface nonlinear properties, where tested by polarization measurements. The polarization plots allowed to identify the bulk and surface contribution to the SHG light. In Fig. 4, the bulk contribution to the SHG light is identifiable in the orthogonal configuration (blue), whereas the surface contribution is identifiable in the parallel configuration (red). In Fig. 4(a), the orientation of

#255882 Received 17 Dec 2015; revised 19 Jan 2016; accepted 19 Jan 2016; published 22 Jan 2016
© 2016 OSA

the crystallographic axes with respect to the measurements is presented. All the polarization measurements were recorded for the average laser pump power of 50mW.

Measurements of the SHG light from the substrate indicate the orientation of the crystallographic axis (Fig. 4(b)) and reveal the four-fold symmetry of the crystal. In fact, in the orthogonal configuration, the contributions $P_x^{(2)}$ (Eq. (1)) for φ_{SHG} = 0°, 180° and $P_y^{(2)}$ (Eq. (2)) for φ_{SHG} = 90°, 270° are clearly visible. In the parallel configuration, instead, the contribution $P_z^{(2)}$ (Eq. (3) is dominant.

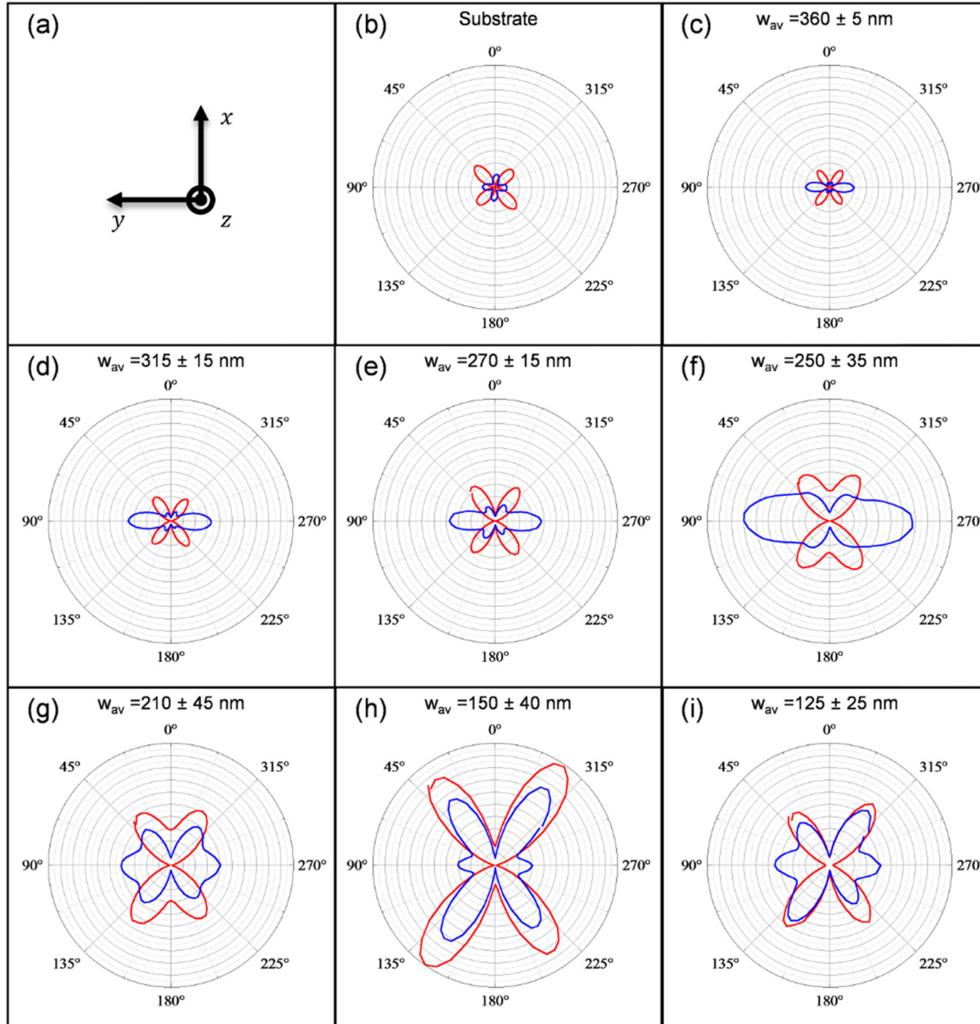

Fig. 4. Polarization plots of SHG light (all in the same scale). In red, parallel configuration, in blue, orthogonal configuration. Laser average power P_{av} = 50mW. The angle represented in the axis is φ_{SHG}. (a) Orientation of the crystallographic axes with respect to the polar plots. (b) Substrate. (c-k) MSW (II) (fabricated at 10 pA FIB current).

In Fig. 4(c)-4(i) the dependence of the intensity and contributions to the SHG light from the different widths of the slab waveguides, in structure (II) (10pA) is shown. Measurements were done after the post-processing step consisting of the laser exposure for less than 5 min. Due to the laser spot diameter (2 μm) the contributions to SHG light are presented for the average waveguides width (w_{av}). The maximum error of the waveguide width (Fig. 4(c)-4(i)) is defined by the smallest and the largest slab in the area covered by the laser spot during the

#255882 Received 17 Dec 2015; revised 19 Jan 2016; accepted 19 Jan 2016; published 22 Jan 2016
© 2016 OSA

measurement. For w_{av} = 250 nm (Fig. 4(f)), the transverse contribution of the bulk, given by $P_y^{(2)}$ (Eq. (2)) for φ_{SHG} = 90°, 270°, is dominant. This is due to a higher value of the field E_z, which indicates the strongest confinement of the electric field. Hence, for w_{av} = 210 nm (Fig. 4(g)), the surface contribution to the SHG light is dominant. This is visible at angles φ_{SHG} = 0°, 180°, indicating contribution from nonlinear polarization component $P_x^{(2)}$. Furthermore, for w_{av} = 150nm (Fig. 4(h)), it is possible to distinguish the dominant longitudinal component ($P_z^{(2)}$). When φ_{PUMP} = 45°, both E_x and E_y contribute to $P_z^{(2)}$ (Eq. (3)). Due to the waveguide geometry, in the far field, $P_z^{(2)}$ is responsible for the SHG polarization normal to the side surfaces of the waveguide. This results in the four lobes being twisted by ± 10° with respect to the substrate (Fig. 4(b)).

In order to investigate the influence of longer laser exposure time (presented in Fig. 3(b)) on waveguide properties, polarization measurements on MSW (II) (50 pA, w_{av} = 280 nm) were performed (Fig. 5) at laser average power of 50 mW. Polarization plots before (a) and after (b) 45 min exposure show at φ_{SHG} = 0°, 180° the surface contribution to the SHG light (in red) reduced to about 20% of the initial value, where at φ_{SHG} = 90°, 270° the bulk contribution to the SHG light (in blue) increased to above 200%. At the same time, the change of the overall shape of the bulk contribution is visible. It is a sign of the modification in the confinement of the light inside the structure. This is attributed to the reduction of the effective waveguide width due to laser-induced local heating effects, resulting in surface oxidation and material redistribution. In addition, the increase of the bulk contribution indicates lower absorption, where decreasing surface contribution is due to the surface oxidization. Note, however, for larger currents (as for 50 pA) the sidewalls of the waveguide are less steep than for the same structure patterned at lower current (10 pA). This results in a smaller waveguide width at the top. Therefore, the plots presented in Fig. 5 have similar shape to the one in Fig. 4(h)-4(i)) corresponding to smaller waveguides, w_{av} = 150 nm and w_{av} = 125 nm.

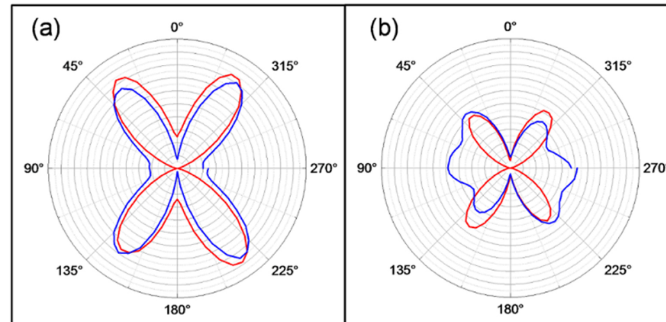

Fig. 5. Polarization plots of SHG light (scale reduced 9 times with respect to Fig. 4) in MSW (II) (fabricated at 50 pA FIB current), w_{av} = (280 ± 10) nm. In red, parallel configuration, in blue, orthogonal configuration. Laser average power P_{av} = 50mW. The angle represented in the axis is φ_{SHG}. (a) before and (b) after the 45 min laser exposure presented in Fig. 3 (b).

Compositional analysis

After the polarization measurements, the samples were investigated with SEM (10 kV, Ultra 55 Gemini, Zeiss). The imaging of the sample revealed the presence of newly formed superficial layer made of nanoparticles (<100 nm), at the same places where the GaP MSW were exposed to the pulsed-laser beam (Fig. 6(a)). In addition, energy dispersive X-Ray (EDS) compositional analysis (10 kV, 2k channels, 60 s, Ultra 55 Gemini, Zeiss) showed a higher presence of oxygen there (Fig. 6(b)).

#255882 Received 17 Dec 2015; revised 19 Jan 2016; accepted 19 Jan 2016; published 22 Jan 2016
© 2016 OSA

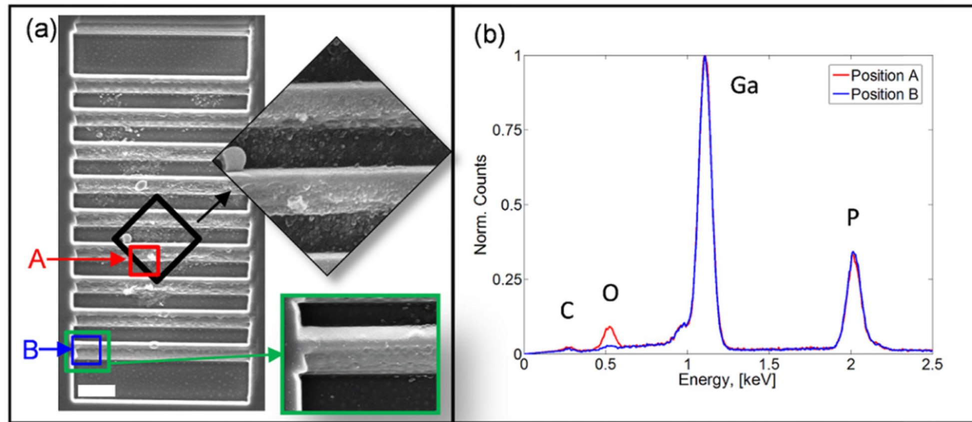

Fig. 6. Compositional analysis of MSW (I). (a) SEM image of the structure. Position A (red) and B (blue) correspond to areas with and without laser exposure, respectively. Scale bar 1µm. (b) Energy dispersive X-Ray (EDS) graph.

To remove the negligible residue of carbon (C) present on the samples (Fig. 6(b)), a cleaning step with oxygen plasma (10 min, 500 sccm of O_2, 1000 W, TePla Model 300 Plasma System) was made. This step did not affect in a substantial way the oxidization of the structures; no oxide layer was found in the areas not exposed to the laser.

Since laser deposition technique has been extensively used for growing oxides, such as gallium oxide (Ga_2O_3) [34–37] and titanium oxide (TiO_2) [35], we attributed the detection of oxygen as the result of gallium oxide formation on the surface. In order to crosscheck the presence of gallium oxide, the samples were immersed in 50% hydrofluoric acid (HF). After 1 min, this process effectively removed the oxide (with the reaction $Ga_2O_3 + 6HF \rightarrow 2GaF_3 + 3H_2O$ [34]), leaving small "cleaning" marks on the surface (Fig. 7(b)). Therefore, laser exposure is the essential step, since the following HF wet etching, is not effective otherwise.

For the structures made with 10 pA, the localized exposure to the laser beam was less than 5 min (as shown in Fig. 3(a)) in order to have a detectable SHG light.

On the other hand, for samples fabricated with higher currents (50 pA) it was not possible to measure any SHG light even after laser exposure times longer time than 5 min. However, in this first exposure, the laser beam stimulated the oxidization of the surface, which was then etched by HF. The same sample was processed similarly once more. Only after that procedure, it was possible to measure the SHG light from the structure. In Fig. 7, it is clearly visible the difference betweenthe surface layers before (a) and after (b) the complete process, consisting of laser exposure, oxygen plasma and HF wet etching. The necessity to perform extra steps in the case of the structure fabricated with higher current can be explained by the higher density and the larger dimensions of the gallium droplets and the higher redeposition rate of the milled material.

Some side effects of using the presented post-process steps were also observed. First, the formation of the gallium oxide continued after the laser exposure. Imaging the samples with the SEM (10 kV, Ultra 55 Gemini, Zeiss) several weeks after the measurements, it was clearly visible that an increased portion of the surface was covered by the gallium oxide. The oxidization was observed also in the areas shortly exposed to the laser, e.g. along the paths from one measurement point to the next. In those cases, the oxidization was not visible just after the measurement. However, the process can be stopped by HF wet etching, since the oxide layer (corresponding to defects inside the GaP structure) is removed. On the other hand, pumping the fabricated structures with higher average laser power (>150mW) or for longer time irremediably damaged the structures.

#255882 Received 17 Dec 2015; revised 19 Jan 2016; accepted 19 Jan 2016; published 22 Jan 2016
© 2016 OSA

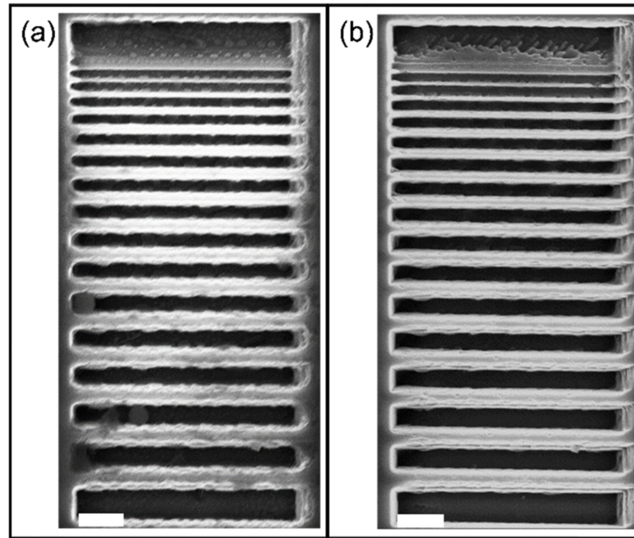

Fig. 7. SEM image of MSW (II) fabricated at 50pA FIB current. Scale bar 1μm. (a) After the fabrication with FIB. (b) After the laser, the oxygen plasma and HF etching.

Conclusions

Multilayer slab waveguides were fabricated on a single-crystal (100) gallium phosphide wafer using focused ion beam milling at 10 pA and 50 pA currents and 30 kV acceleration voltage. This process gave good quality structures (smallest features 30 nm with aspect ratio 20:1) but with superficial droplets of gallium, which limited the optical properties of the waveguides. To solve this problem, a pulsed-laser beam at 150mW was used to expose the nanostructures surface and convert the gallium-rich surface into gallium oxide. In order to test the quality of the structures for potential applications in nanophotonics, we analysed the second-harmonic generation response. For the structure patterned at 10 pA and laser exposure of less than 5 min, we could observe bulk and surface contributions to the optical nonlinearity. Interestingly, for the structure patterned at 50 pA, the repetition of the process consisting of pulsed-laser exposure, oxygen plasma and wet etching with hydrofluoric acid, was required to improve the quality of the waveguides. Moreover, while a longer laser exposure duration reduced the optical losses further, it also increased surface oxidation thereby decreasing the surface optical nonlinearity. Furthermore, the presented method can be used as a post-process technique to recover the nanostructures fabricated in III-V materials with focused ion beam. The reported method and the possibility to monitor the oxidization on the surface can open doors to a variety of different applications which require high aspect ratio structures in III-V materials or gallium oxide nanoparticles on complex structures.

Acknowledgments

The work was performed within the Linné Center for Advanced Optics and Photonics (ADOPT). Support from the Swedish Research Council VR (grant numbers, 349-2007-8664 and 621-2013-5811) are acknowledged.

#255882 Received 17 Dec 2015; revised 19 Jan 2016; accepted 19 Jan 2016; published 22 Jan 2016